

# Vortices in two-effective-band, stoichiometric high $T_c$ $\text{CaKFe}_4\text{As}_4$ superconductor

Antón Fente,<sup>1</sup> William R. Meier,<sup>2,3</sup> Tai Kong,<sup>2,3</sup> Vladimir G. Kogan,<sup>2</sup>  
Sergey L. Bud'ko,<sup>2,3</sup> Paul C. Canfield,<sup>2,3</sup> Isabel Guillelmo,<sup>1</sup> and Hermann Suderow<sup>1</sup>

<sup>1</sup>*Laboratorio de Bajas Temperaturas y Altos Campos Magnéticos,  
Unidad Asociada UAM/CSIC, Departamento de Física de la Materia Condensada,  
Instituto de Ciencia de Materiales Nicolás Cabrera and Condensed Matter  
Physics Center (IFIMAC), Universidad Autónoma de Madrid, Spain*

<sup>2</sup>*Ames Laboratory, Ames, IA 50011*

<sup>3</sup>*Department of Physics & Astronomy, Iowa State University, Ames, IA 50011*

(Dated: August 3, 2016)

Many single crystalline iron based superconductors can be understood by considering a superconducting order parameter that changes sign in two different parts of the Fermi surface. Interband scattering in such  $s\pm$  superconductors is expected to considerably modify the superconducting density of states at the Fermi level close to crystalline defects, as a consequence of the sign changes of the order parameter. Unlike other known superconductors, vortex lattices in single crystals of iron based superconductors are often disordered. However, it is still unknown if these disordered vortex lattices are due to defect scattering or to substitutional disorder. Here we study single crystals of stoichiometric  $\text{CaKFe}_4\text{As}_4$ . The superconducting critical temperature is very high, of  $T_c = 35$  K, a value comparable to that found near optimal substitution levels in disordered iron based systems. Using a scanning tunneling microscope we find two-gap superconducting behavior. We observe that the vortex lattice is hexagonal but becomes disordered after a few lattice spacings. We find that the spatial variation of the superconducting order parameter within a vortex core is the same in the two parts of the Fermi surface. Disorder in the vortex lattice appears because vortices tend to be located at positions where scattering by defects induces a finite density of states at the Fermi level.

## I. INTRODUCTION

The high critical temperature  $T_c$  and upper critical field  $H_{c2}$  of iron based superconductors make them promising materials for applications [1]. The highest  $T_c$ 's of Fe based materials appear in doped systems with substitutional disorder [2–6]. These are multiband systems with different bands crossing the Fermi level. In general, it is believed that the superconducting order parameter has  $s$ -wave symmetry but changes sign between different bands, giving  $s\pm$  superconductivity, within a scenario involving two effective bands. In this kind of superconductor, interband scattering due to defects occurs between bands having order parameter components of opposite sign and leads to a finite density of states at the Fermi level around defects and eventually to pair breaking at high defect concentration with a reduced critical temperature [5, 7–10].

Often, vortex lattices of type II superconductors can be disordered in presence of pinning by all kinds of inhomogeneities. In the Fe based systems, imaging experiments nearly always show disordered vortex lattices beyond a few lattice spacings [11–13]. However, the sources for pinning have not been unambiguously identified. In the stoichiometric system,  $\text{LiFeAs}$ , vortex lattice disorder has been observed, but has been related to the softening of the vortex lattice when increasing the magnetic field, and the origin of pinning remained unclear [14, 15]. In other systems, the presence of substitutional disorder introduced by doping makes it difficult to identify the origin for vortex pinning. The question of how scattering by defects contributes to pinning remains unsolved. To ad-

dress this question, we study here the recently discovered, stoichiometric,  $\text{CaKFe}_4\text{As}_4$  superconductor [16, 17] with  $T_c \cong 35$  K using Scanning Tunneling Microscopy (STM). Contrary to the much studied  $(\text{Ba}_{1-x}\text{K}_x)\text{Fe}_2\text{As}_2$  systems, where Ba and K are distributed randomly in the lattice, in  $\text{CaKFe}_4\text{As}_4$  Ca and K occupy alternatively different positions between  $\text{Fe}_2\text{As}_2$  layers. We find two-gap superconducting features consistent with  $s\pm$  superconductivity, determine the superconducting coherence length and image the vortex lattice as a function of the magnetic field. We find that defects and isolated areas showing a finite density of states at zero field provide vortex pinning and thereby cause the vortex lattice disorder.

The recently grown single crystals of  $\text{CaKFe}_4\text{As}_4$  [17] show low residual resistivity, no sign of a structural phase transition below room temperature and an upper critical field  $H_{c2}$  above 70 T [17]. Penetration depth and tunneling experiments show evidence for two well defined superconducting gaps and sign changing behavior in agreement with  $s\pm$  superconductivity [18]. Results are comparable to optimally doped  $(\text{Ba}_{1-x}\text{K}_x)\text{Fe}_2\text{As}_2$ . The band structure of is also similar to that of  $(\text{Ba}_{1-x}\text{K}_x)\text{Fe}_2\text{As}_2$  compounds, with three hole pockets at the  $\Gamma$  point and two electron pockets at the  $M$  point [19]. The gap values from angular resolved photoemission vary significantly for different pockets, with a large gap for pockets that have similar size at  $\Gamma$  and  $M$  points and a smaller gap for a Fermi surface of larger diameter at the  $\Gamma$  point, suggesting enhancement of superconductivity by nesting. This shows that two-gap features are due to superconducting gap values in well separated bands, and favors  $s\pm$  superconductivity due to repulsive electronic interband

interaction[18, 19].

We have done our experiments using a home-made STM at temperatures of 0.8 K and under magnetic fields up to 8 T. Details of the set-up are given in the Appendix. We cleave the sample in-situ, leaving clean surfaces parallel to the basal plane of the tetragonal crystal structure. We find almost atomically flat and large surfaces, showing atomic size (2-3 Å) steps (Fig.1). These almost flat surfaces are separated by larger steps of integer or half-integer values of the c-axis lattice constant ( $c = 12.88$  Å[19]). We provide more details of the topography in the Appendix, and focus here on the spatial distribution of the superconducting tunneling conductance.

## II. TWO-GAP SUPERCONDUCTIVITY AT ZERO MAGNETIC FIELD

Tunneling conductance shows clear superconducting features over the whole surface (Fig.1), from which we obtain two characteristic gap values,  $\Delta_1 = 3$  meV  $= 0.6\Delta_0$  and  $\Delta_2 = 8$  meV  $= 1.5\Delta_0$  (with  $\Delta_0 = 1.76k_B T_c$ ). The relative weight of the superconducting features corresponding to each gap varies slightly across steps of atomic height (Fig.1). The observed flat surfaces with stripe-like atomic size steps are actually very similar to results in  $(\text{Ba}_{0.6}\text{K}_{0.4})\text{Fe}_2\text{As}_2$  [20]. The spatial dependence of the weight of the different gap features on the tunneling conductance is similar too. This shows that the contribution of different parts of the Fermi surface to the tunneling conductance changes as a function of the atomic plane into which we are tunneling, because in each surface the tunneling matrix elements, linked to the terminating surface atoms, are different[13, 20, 21].

Previous results for LiFeAs and in  $(\text{Ba}_{1-x}\text{K}_x)\text{Fe}_2\text{As}_2$  also show two-gap features in the tunneling conductance. In  $(\text{Ba}_{1-x}\text{K}_x)\text{Fe}_2\text{As}_2$  and in similar doped compounds, maps of the superconducting density of states show strong variations, including changes in the gap distribution and depression of superconducting features with an increase in the zero bias conductance [13, 14, 22]. This has been associated with the distribution of dopants in the sample[23]. Here in stoichiometric  $\text{CaKFe}_4\text{As}_4$ , we find a vanishing zero bias tunneling conductance over large areas, as in LiFeAs[14]. However, we also find isolated areas where defects produce a finite density of states at the Fermi level. These will be discussed below.

## III. $\text{CaKFe}_4\text{As}_4$ UNDER MAGNETIC FIELDS: VORTEX CORE AND LATTICE

As magnetic field is applied to  $\text{CaKFe}_4\text{As}_4$ , a vortex lattice appears over the whole surface. In Fig.2 we show vortex lattice images from 1 T to 8 T taken in different scanning windows. The vortex lattice is hexagonal, as shown by the autocorrelation functions (lower right insets in each image of Fig.2). The magnetic field dependence of

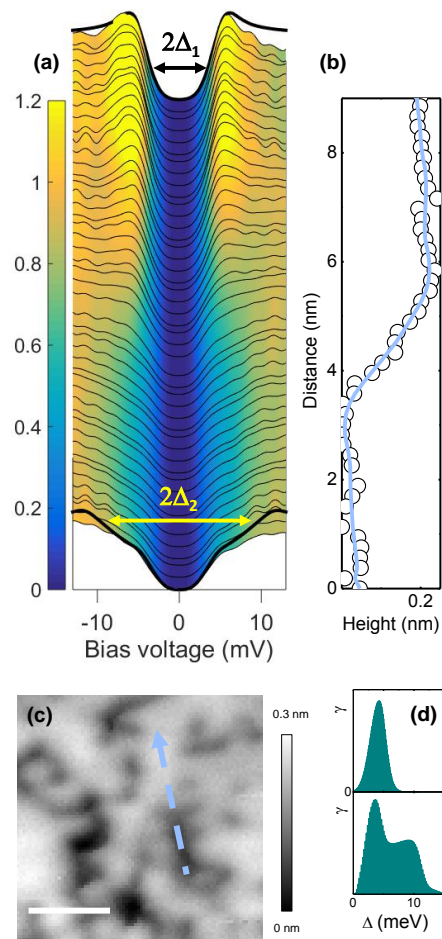


FIG. 1. (a) Line scan over an atomically flat area. Color scale presents the normalized conductance values given by the bar in the left of the panel. We mark by arrows the main values of the superconducting gap found, as discussed in the text,  $\Delta_1$  and  $\Delta_2$ . (b) Height profile along the line scan shown in (a). The blue line is a guide to the eye. (c) Typical topography of an almost atomically flat area. The difference between black and white is given by the bar on the right of the panel. The arrow shows the line used to make the scan shown in (a). The white bar is 4 nm long. (d) Distribution of gap values  $\Delta$  being the gap values and the relative weight of the corresponding gap values  $\gamma$ . Using the distributions of states shown in the figure, we generate a superconducting density of states summing over all gaps with the corresponding weights, that is  $\sum_{\Delta_i} \gamma_i \frac{E}{E^2 - \Delta_i^2}$ . We convolute the resulting density of states with the derivative of the Fermi function to find the tunneling conductance given by the black lines at the top and bottom of the panel in (a).

the intervortex distance  $d$  is as expected for a hexagonal vortex lattice,  $d^2 = 2\Phi_0/\sqrt{3}H$ ,  $\Phi_0$  is the flux quantum. The vortex lattice shows short range order with defects in the hexagonal arrangement appearing every few lattice spacings. We discuss this below and focus first on the shape of the vortex cores.

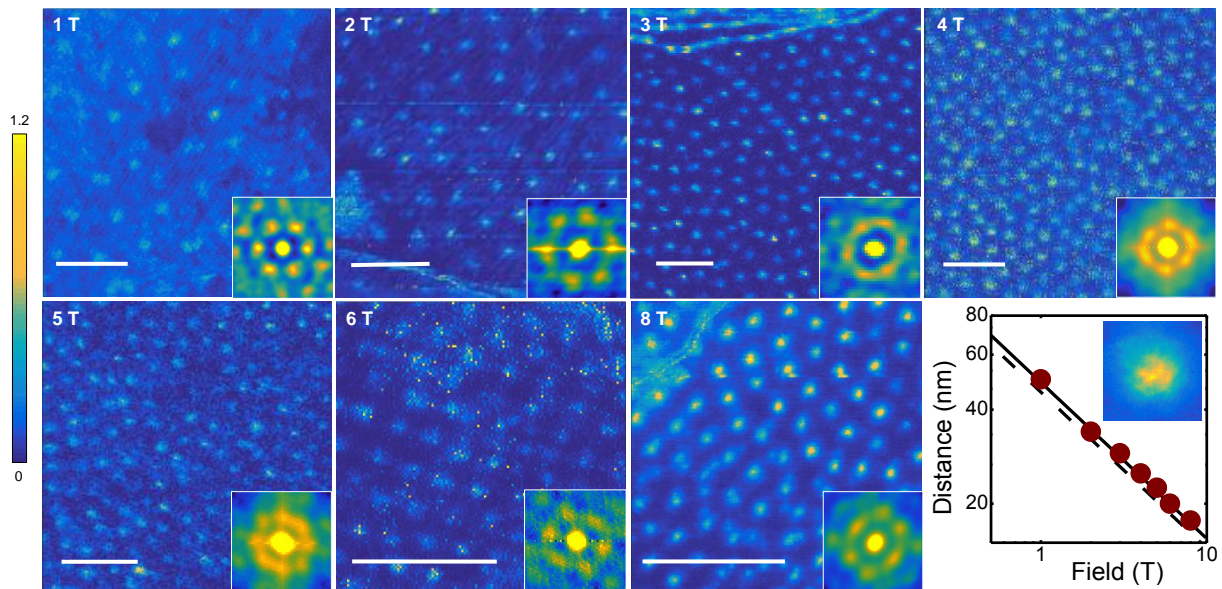


FIG. 2. Zero bias conductance maps in fields between 1 T and 8 T taken at different positions. The color bar on the left provides the zero bias normalized tunneling conductance. The white bar in the images is of 82 nm size. The insets in the images show the autocorrelation function of the images. Note that the lattice remains hexagonal, within first nearest neighbors, over the whole magnetic field range. The lower right panel shows the intervortex distance, obtained from the autocorrelation function, vs the magnetic field and the black lines are the expected intervortex distance for hexagonal (solid line) and square (dashed line) lattices; the inset shows the zero bias conductance map of an isolated vortex.

### A. Vortex cores

Vortex core shape provides a measurement of the anisotropy of the electronic properties in the plane perpendicular to the magnetic field[21, 24]. Vortex cores are generally round in  $\text{CaKFe}_4\text{As}_4$  (Fig.2), showing no sizeable in-plane anisotropy. In FeSe, strong in-plane electronic anisotropy produces elongated vortex cores[13, 25]. In LiFeAs, a four-fold anisotropy has been reported[14]. In the doped Fe pnictides, vortex cores are often round, although it is not clear if this is due to defect scattering or if it is an intrinsic property of the material itself[13]. The result found here in stoichiometric  $\text{CaKFe}_4\text{As}_4$  shows that anisotropies in the in-plane gap and Fermi surface of  $\text{CaKFe}_4\text{As}_4$  are small, in agreement with recent angular resolved photoemission spectroscopy measurements[19].

In Fig.3 we show the normalized tunneling conductance as a function of the distance from the vortex core, in units of half the intervortex distance at each magnetic field (see the Appendix for details on the normalization procedure). Each curve is obtained from the angular average of the normalized tunneling conductance vs distance from the vortex center  $r$ . We find that the shape of the normalized conductance curves does not change much with the magnetic field up to 8 T. As shown in Ref.[26], the distribution of the density of states within the vortex lattice can be related to the superconducting order parameter  $\Delta_{OP}(r)$  following de Gennes. Authors of Ref.[26] combine this with an established Ansatz for the radial de-

pendence of the order parameter  $\Delta_{OP}$  and the Wigner-Seitz approximation for the periodic vortex lattice to obtain the density of states as a function of the core size  $C$ . The core size is defined as  $C_i \propto (d\Delta_{OP,i}/dr|_{r \rightarrow 0})^{-1}$ , where  $\Delta_{OP,i}$  is the order parameter in each band[26].  $C_i$  is obtained by fitting the data in Fig.3 to the analytical expressions given in Ref.[26] where  $C_1$  and  $C_2$  are the only free parameters. From the data fits, we find that we need to use the same values of  $C_i$  for each band, except at 8 T, where we obtain a small difference (open point in Fig.3). We compare the measured  $C_i$  with the behavior expected for a superconductor in the clean limit,  $C_i \propto 1/\sqrt{H}$  (in the dirty limit,  $C$  is expected to be field independent[26]). Although at low fields the data are somewhat below the proposed behavior, given the crude approximations involved in the formalism, we consider this to be a good agreement. When we extrapolate  $C_i$  up to  $H_{c2}$  (around 70 T), we find a value for the coherence length  $\xi$  of 1.8 nm, which is close to the value obtained previously from  $H_{c2}$  (2 nm, using  $\xi \approx \sqrt{\frac{\phi_0}{2\pi H_{c2}}}$ ) [17]. Thus, in  $\text{CaKFe}_4\text{As}_4$  the core shrinks with magnetic field, as expected for clean superconducting materials [27, 28].

There are available results for comparison to other two-band superconductors, the dichalcogenide systems  $2\text{H-Nb}(\text{Se}_{1.98}\text{S}_{0.02})$  and in  $2\text{H-NbS}_2$ [26]. In  $2\text{H-NbSe}_{(1.98}\text{S}_{0.02)}$ ,  $C_i$  is independent of the magnetic field, compatible with this material being close to the dirty limit. A similar behavior was also observed in clean crystals of  $2\text{H-NbS}_2$ , suggesting that the scattering might be



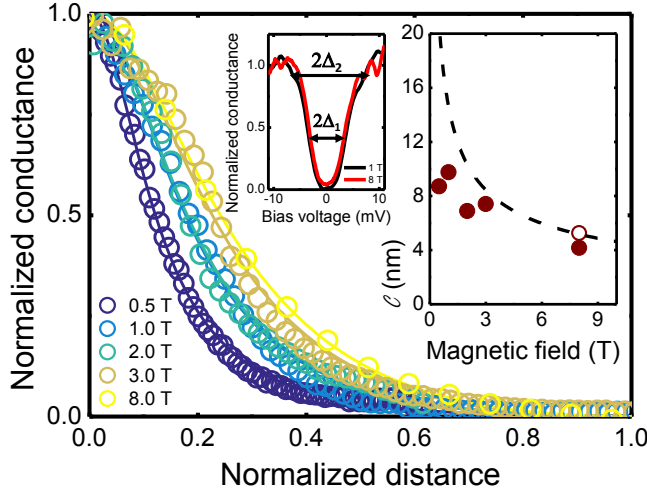


FIG. 3. The normalized tunneling conductance vs normalized distance for different magnetic fields. The tunneling conductance is normalized as to provide unity in the vortex center and zero at Wigner-Seitz cell boundary. The distance  $r$  is normalized by half the intervortex distance at each magnetic field (further details are given in Appendix). In the inset at the center we show the tunneling conductance at 1 T (black curve) and 8 T (red curve) in between vortices. In the inset at the right we show the vortex size  $C_{1,2}$ , defined in the text, as a function of the magnetic field (points). We find  $C_1 = C_2 = 8.7; 9.8; 6.9; 7.4$  up to 3 T and  $C_1 = 4.2$  (filled circle) and  $C_2 = 5.3$  (open circle) at 8 T. The dashed line is  $\propto \sqrt{1/H}$  and extrapolates to 1.8 nm at the  $H_{c2}$  found in macroscopic measurements, which is above 70 T [17].

band dependent in this material. As in both of these two-gap systems, here in  $\text{CaKFe}_4\text{As}_4$  we also obtain the same vortex core size  $C_i$  for parts of the Fermi surface with different gaps. The difference between gap magnitudes is considerably larger in  $\text{CaKFe}_4\text{As}_4$ , strengthening the suggestion made in Ref.[26] that the length scales are the same for the spatial variation of the different components of the order parameter in these multigap superconductors.

In  $\text{CaKFe}_4\text{As}_4$ , the tunneling conductance is very similar at zero field and in fields up to 8 T between vortices. In phonon-mediated two-gap superconductors, such as  $\text{MgB}_2$  and dichalcogenides  $2\text{H-Nb}(\text{Se}_{1.98}\text{S}_{0.02})$  and  $2\text{H-NbS}_2$ , the zero bias conductance strongly increases when the field is below a tenth of  $H_{c2}$  [29–33]. In  $\text{MgB}_2$ , for instance, small magnetic fields provide a sizeable reduction of the component of the order parameter in the part of the Fermi surface having the smaller sized gap. However, in  $\text{LiFeAs}$ , the tunneling conductance in between vortices does not differ considerably from the zero field result up to magnetic fields of about 9 T (about half  $H_{c2}$ ). In  $\text{CaKFe}_4\text{As}_4$  all parts of the Fermi surface remain gapped in magnetic fields below 8 T (upper inset of Fig.3). Macroscopic  $H_{c2}$  and penetration depth mea-

surements show that the interband coupling is strong in  $\text{CaKFe}_4\text{As}_4$  and in  $\text{LiFeAs}$ [17, 18]. This suggests that interband coupling influences the magnetic field behavior of iron pnictide materials giving gap features that remain magnetic field insensitive in between vortices.

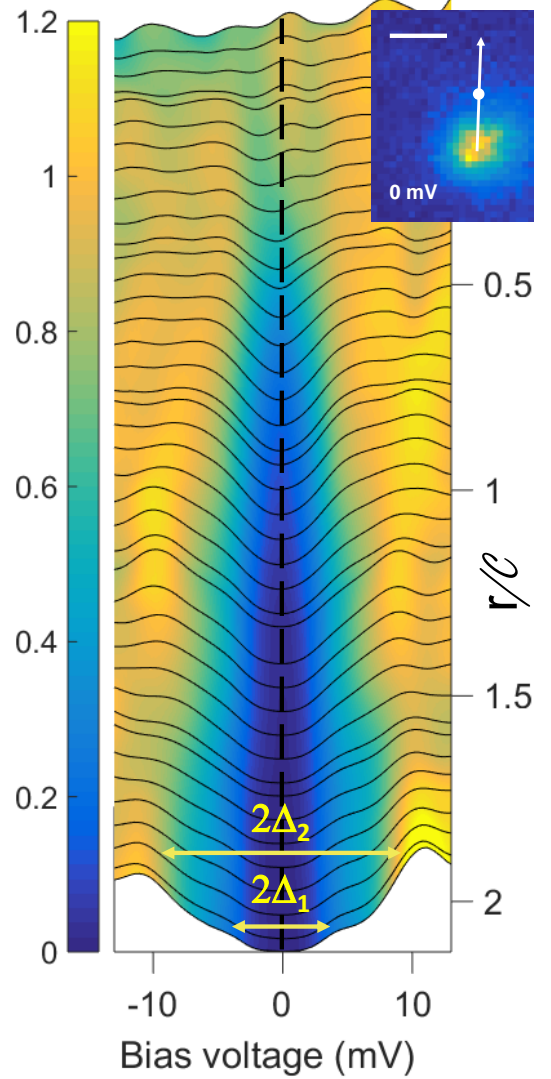


FIG. 4. The normalized tunneling conductance curves at 1 T, along the white line shown in the inset at the right top, which goes from the vortex center to an area in between vortices. White dot marks the size of  $C$ . The scale at the right provides the distance from the vortex center in units of  $C$ . Note the evolution from a small near zero bias peak at the vortex center into the two-gap normalized tunneling conductance away of the center.

The evolution of the tunneling conductance from the vortex core to the gapped region in between vortices is shown in Fig.4. Results are similar for all magnetic fields. We find tunneling conductance curves showing a peak close to zero bias in the vortex core (we discuss this in the Appendix). There is a gradual evolution from the asymmetric shape and increased conductance close to zero bias

to the two-gap tunneling conductance in between vortices (in Fig.4 we present a line scan without crossing the atomic size steps leading to the changes discussed in Fig.1, in the Appendix we provide other results). It is worth pointing out that the superconducting features are established at a distance from vortex center of order of  $C_i$ .

## B. Vortex lattice

Now we discuss the behavior of the vortex lattice. First, we note that the autocorrelation functions provide six-fold symmetric features, indicating that the underlying order is hexagonal over the whole magnetic field range studied. However, the position of vortices is strongly influenced by defects in a given area. In Fig.5 we show the image taken at 4 T and its Delaunay triangulation[34]. The ratio of defects in the vortex lattice is very high, with roughly the same number of five-fold and seven-fold vortices, that sums up to nearly the number of vortices with six nearest neighbors. This is expected for a disordered vortex lattice[34]. We can identify small areas with hexagonal order, separated by lines of dislocations (pairs of five and seven fold vortices).

To discuss this in more detail, we present in Fig.6 a map of the tunneling conductance at different bias voltages at 1 T in an area with a particularly large amount of defects. The expected amount of vortices in the area shown is about 36. We identify 22, arranged in a rather disordered way. The rest is located in larger areas with an increased zero bias conductance and are more difficult to identify. This often occurs close to step edges of large size that are particularly numerous in Fig.6. We can roughly link the size of small ordered areas with the separation among features found in the topography, of order of several tens of nm.

In the image at 1 T shown in Fig.6, out of the 22 vortices seen, only 6 are located in areas with a negligible zero bias conductance. Most of them are located along the light blue lines seen in the zero bias conductance image. In areas with a smaller amount of defects, this results in vortex lines. For example, the vortices joined by a finite zero bias conductance as in the upper part of the image at 3 T shown in Fig.2. Another example is found in the image at 4 T shown in Fig.5, the feature found in the upper left part of the image is a large step which shows a high zero bias conductance. Probably, the step is full of vortices, but these are difficult to identify. The lines with a finite zero bias conductance are also observed in the conductance maps taken at zero magnetic field (see Appendix) at step edges or other identifiable features in the topography.

From the tunneling conductance maps made at finite bias voltages shown in Fig.6 we observe a strong increase in the tunneling conductance in between the lines where vortices are located. This increase appears already well within the smaller sized superconducting gap  $\Delta_1$ . In par-

ticular close to the lines where we observe a finite zero bias conductance. Even if the conductance at non-zero bias is finite over large parts of the image, vortices prefer the locations with finite zero bias conductance.

We thus conclude that the disorder in the vortex lattice is due to pinning at positions where defects induce a finite zero bias conductance.

Much theoretical work focuses on the particular sensitivity of sign changing superconductors to scattering by defects[8]. Within  $s\pm$  superconductivity, a finite Fermi level density of states can appear at any defect producing scattering between bands with order parameter components of opposite sign.

Previous measurements in the pnictides include STM in Fe(Se,Te), where isolated Fe impurities provide a zero bias peak. The authors could not associate the zero bias peak pair breaking effects to  $s\pm$  superconductivity but pointed rather out that there might be strong modifications of the local electronic structure, associated with some form of short range magnetism[35]. When Fe(Se,Te) is irradiated by heavy ions, columnar defects appear as regions with an amorphous crystal structure, where superconductivity is fully suppressed[11]. In LiFeAs, in-gap states are found at native defects on the surface, sometimes with small increases in the zero bias conductance[36, 37]. In FeSe, twin boundaries have been shown to suppress superconductivity, an effect that has been associated with local variations in the atomic arrangement of the Fe-Se blocks close to the twin boundaries[12]. In  $\text{CaKFe}_4\text{As}_4$ , the formation of magnetic moments that might give short range pair breaking is unlikely, because there is no signature for magnetism in macroscopic measurements [17]. In this compound, there are two Fe-As layers with interstitial atoms alternating between Ca and K. Modifications of the FeAs blocks close to defects are quite likely and might produce local suppression of superconductivity. This explains the pair breaking we find at areas with large amounts of defects or step edges. But it cannot easily explain the observed appearance of a zero bias conductance only slightly different from zero at lines or around isolated defects. We associate the latter with scattering between order parameter components of opposite sign, i.e., within  $s\pm$  superconductivity.

The symmetry of the vortex lattice has been studied by STM in several iron based superconductors including some stoichiometric materials such as LiFeAs. Experiments on doped 122 compounds report varied behavior. Vortex lattice images on  $(\text{Sr}_{0.75}\text{K}_{0.25})\text{Fe}_2\text{As}_2$  [25] and  $\text{Ba}(\text{Fe}_{0.9}\text{Co}_{0.1})_2\text{As}_2$  [22] show a disordered vortex lattice while  $(\text{Ba}_{0.6}\text{K}_{0.4})\text{Fe}_2\text{As}_2$  [20, 25] presents a more ordered lattice for the same values of the magnetic fields. This indicates that charge doping by itself does not explain the origin of vortex pinning in these materials. Instead, it has been suggested that electronic inhomogeneity induced by ion size mismatch between substituted elements accounts for the different pinning strengths found in these compounds (for instance, the mismatch between K and

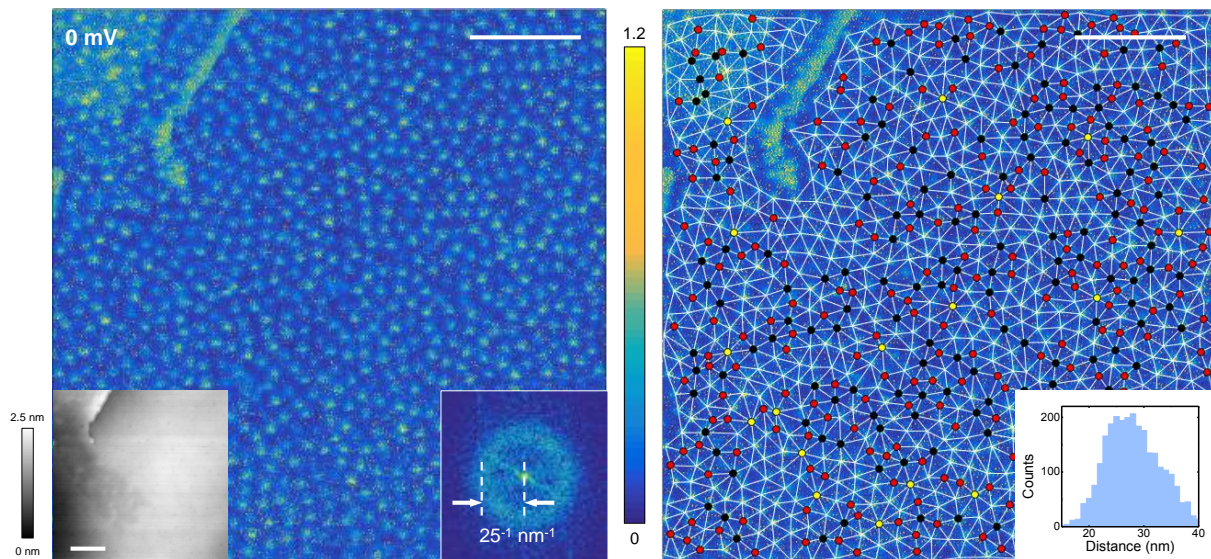


FIG. 5. Left panel: the zero bias normalized conductance map at 4 T, with the scale provided by the color bar on the right. Lower left inset: the topography, with a change in height of 2.5 nm from black to white. The lower right inset: the Fourier transform, which is essentially a circle whose reciprocal space size corresponds to an intervortex distance of 25 nm, as expected for this magnetic field. The right panel: the Delaunay triangulation of the image, made as explained in Ref.[34]. Vortices marked in red have five nearest neighbors (230 vortices), and vortices marked in black seven nearest neighbors (170). A few (17) vortices have eight nearest neighbors and are marked in yellow and the rest (430) have six nearest neighbors. In the lower right panel we show a histogram with the intervortex distances. White bars in the images are 150 nm in length.

Ba is five times smaller than between K and Sr). In bulk Fe(Se,Te) irradiated by heavy ions, vortices are pinned to the amorphous regions at the columnar defects created by irradiation, leading to a complicated pinning landscape [11]. In FeSe, vortices are preferentially positioned near twin boundaries where superconductivity is strongly suppressed[12]. In the stoichiometric pnictide LiFeAs a very disordered vortex lattice has been observed in absence of twin boundaries or substitutional disorder but at much larger values of  $H/H_{c2}$ , where vortex disorder due to lattice softening is much more significant [14]. The present results in stoichiometric CaKFe<sub>4</sub>As<sub>4</sub> evidence pinning at positions where defects produce a finite density of states at the Fermi level, explaining the disorder in the vortex lattice.

#### IV. CONCLUSIONS AND OUTLOOK

By measuring single crystals of the newly found high  $T_c$  superconductor CaKFe<sub>4</sub>As<sub>4</sub> we show that vortex pinning is unambiguously associated with a finite density of states at the Fermi level due to defect scattering. We show that two-gap features are robust to the magnetic field and measure the superconducting coherence length, consistent with the huge  $H_{c2}$  of this material[17]. The disordered vortex lattice characteristic of  $s\pm$  pnictide superconductors is due to the inherent sensitivity of  $s\pm$  superconductivity to defect scattering. CaKFe<sub>4</sub>As<sub>4</sub> opens

new prospects to understand the main properties that lead to high critical magnetic fields in the Fe based systems.

#### V. ACKNOWLEDGMENTS

We acknowledge discussions with R. Prozorov and S. Vieira. Work done in Madrid (AF, IG and HS) was supported by the Spanish Ministry of Economy and Competitiveness (FIS2014-54498-R, MDM-2014-0377), by the Comunidad de Madrid through program Nanofrontmag-CM (S2013/MIT-2850), by EU (FP7-PEOPLE-2013-CIG 618321, Cost MP-1201) and by Axa Research Fund. IG acknowledges the European Research Council (PNICTEYES project, grant agreement 679080). SEGAINVEX-UAM and Banco Santander are also acknowledged. Work done in Ames Lab (PCC, SLB, VGK, TK) was supported by the U.S. Department of Energy, Office of Basic Energy Science, Division of Materials Sciences and Engineering. Ames Laboratory is operated for the U.S. Department of Energy by Iowa State University under Contract No. DE-AC02-07CH11358. W. M. was supported by the Gordon and Betty Moore Foundations EPiQS Initiative through Grant GBMF4411.



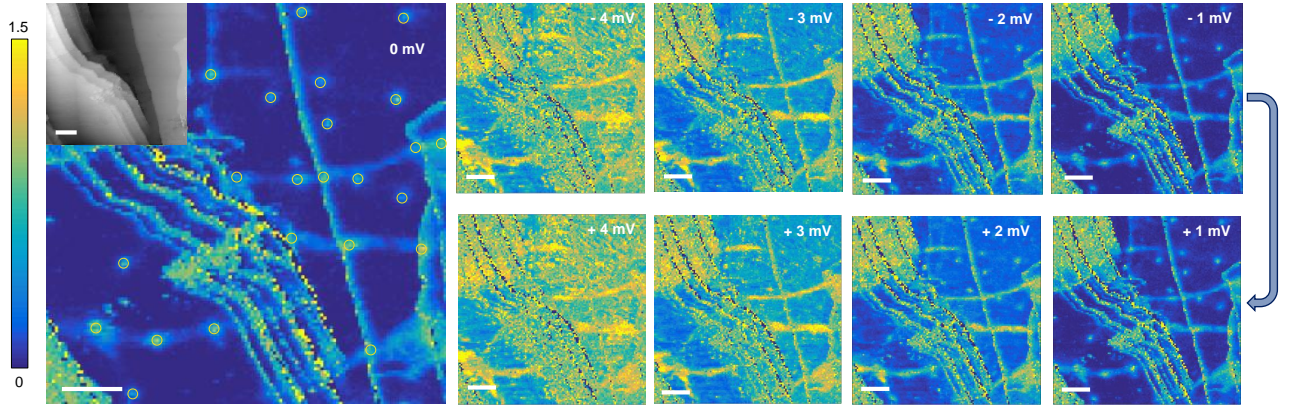


FIG. 6. The main panel at the left: the zero bias conductance map at 1 T; the topography of the mapped area is shown in the upper left inset of the panel. The height difference in the topography image is of 25 nm from black to white. We observe 22 vortices, marked by yellow circles. The series of panels on the right: conductance maps at different bias voltages, marked in each figure. White bars are 50 nm in size and the color provides the normalized conductance according to the bar shown at the left of the figure.

## VI. APPENDIX

### A. Topography and surfaces of $\text{CaKFe}_4\text{As}_4$ .

In Fig.7 we show a large area which is useful to discuss the main features of the surface of  $\text{CaKFe}_4\text{As}_4$  and related these to previous findings in Fe based superconductors.

The zooms in the upper left and right panels provide the typical images found at the surface of  $\text{CaKFe}_4\text{As}_4$ . The surfaces are flat down to fractions of a nm with, however, no visible atomic lattice on them. Instead, we observe small stripes as shown in upper left and right panels of Fig.7. Quite often, these areas are interspersed with small round features. The step edge between the surface layer and the layer within the round features is just of 0.2 nm, that is, of atomic size. Within the same image we also show a large area with a surface reconstruction (bottom right panel of Fig.7). In the rare reconstructed surfaces we see no superconducting features. This reminds the features largely discussed in the literature of STM in the Fe-based materials[13].

In the  $\text{AFe}_2\text{As}_2$  based materials (A being for instance Ba, K or Ca), the sample cleaves in between FeAs blocks, leaving the A lattice exposed. It turns out that the square A lattice is not stable, and most studied  $\text{AFe}_2\text{As}_2$  materials show a reconstruction, consisting of stripes due to arrangements of half of the A atomic lattice. Indeed, half of the A atomic lattice is left in the sample and the other half is taken away at the cleaving procedure [13]. In some particular cases [23, 38], it has been possible to image the As lattice, although most of the surface is covered by stripes of A atoms due to the reconstruction. The superconducting gap does not, generally, appear in the reconstructed areas (with some exceptions, see [13]), indicating that these areas have either pair breaking ef-

fects or considerably modify the electronic structure of the surface layers.

The  $\text{CaKFe}_4\text{As}_4$  system takes advantage of the regular spacing between Ca and K atoms and their different atomic radii to release the steric pressure of the Ca ions, which is known to be very large and leads to important strain related effects in the doped  $\text{CaFe}_2\text{As}_2$  system[39]. It is reasonable to assume that the cleaving in  $\text{CaKFe}_4\text{As}_4$  occurs also in between Fe-As blocks, as in the  $\text{AFe}_2\text{As}_2$  systems. However, the lattice is much less strained now, so the sample will almost certainly cleave differently. Our observation of having most of the surface without the linear reconstruction often found in these materials shows that this is indeed the case.

We can now discuss the surface termination in our images. The rare reconstructed areas observed in Fig.7 are places where only half of either Ca or K atoms have been left at the surface. Otherwise, the Ca or K atoms can form nearly full layers on the surface, without the linear surface reconstruction found in other materials. The stripe like features seen then preferentially over the surface (upper left and right panels of Fig.7) are possibly missing rows of alkali (K) and alkaline-earth (Ca) atoms. The holes seen on those surfaces are places with small sized surfaces having only half of the Ca or K atoms and showing the row like structure characteristic of the reconstruction (bottom left panel of Fig.7).

### B. Superconducting tunneling conductance and defect scattering at zero field

The surface topology has distinct consequences on the observation of superconducting features in the tunneling conductance. In Fig.8 we show an area where there is one step roughly of unit cell size. The image has been

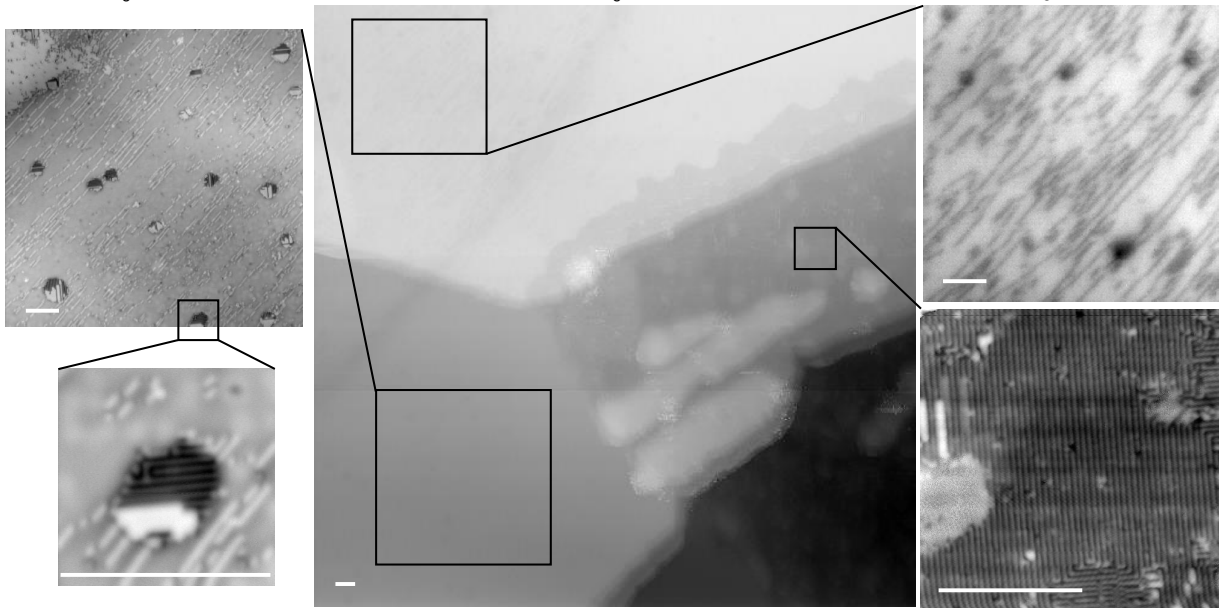


FIG. 7. Typical features in the topography as measured by STM of  $\text{CaKFe}_4\text{As}_4$ . Scale is given by the white bars in every panel, of 20 nm size. In the main panel (5.6 nm change in height from black to white) different areas are seen. We have chosen the contrast to highlight three different areas, leaving the black triangle on the bottom right out of the discussion. The upper right and upper left panels provide a zoom on two of these areas. These are most frequently observed on the surface of the sample. The top left image shows a contrast from black to white of 0.85 nm. The top right image of 0.3 nm. In the top left image, we make an additional zoom into a small hole like defect and show the zoom in the bottom left image. The height difference in this image (from white to black) is of 0.5 nm, that is, of just two atoms. The bottom right image is a zoom on an area where we observe a surface reconstruction. This is rarely observed on the surface of the sample.

taken at zero magnetic field. The zero bias conductance maps show actually a negligible density of states close to the Fermi level over most of the surface. The tunneling conductance shows an extended and smeared density of states, with two characteristic gap features far from the step edge. The step edge produces a finite density of states at the Fermi level, with an increased zero bias conductance along the whole step. Enhanced scattering along the step leads to a line with pair breaking through scattering between wavefunctions of opposite sign.

On the other hand, there are also places in the image with an accumulation of hole defects like the ones shown in lower left panel of Fig.7. In the upper left part of the image in Fig.8, an accumulation of such holes leads to round like features. At these places, we also observe a finite zero bias conductance (lower left panel of Fig.8). Two-gap features are still observed in the tunneling conductance.

### C. Vortex core states

The normalized tunneling conductance at the vortex center shows a small peak for positive bias voltages, as shown in Fig.4. We find values for the normalized tunneling conductance of at most 1.2 at the peak. This value is considerably below the value found in the vortex centers

of  $2\text{H-NbS}_2$  or  $\text{YNi}_2\text{B}_2\text{C}$ , that are closer to 1.5[40–43]. Still, the conductance has an identifiable peak at a positive bias voltage in  $\text{CaKFe}_4\text{As}_4$ .

We can discuss this feature in terms of quantized vortex core levels predicted by Caroli, de Gennes and Matricon for clean superconductors[21, 24, 44]. The lowest core level has a zero point energy of about  $\Delta^2/2E_F$  (with  $\Delta$  the superconducting gap and  $E_F$  the Fermi energy). This is practically negligible in conventional superconducting materials, the usual observation being a zero bias peak in the tunneling conductance [40, 41, 43]. In  $\text{CaKFe}_4\text{As}_4$  we observe a slightly asymmetric peak close to zero bias, but not exactly at zero bias (at a positive bias, see Fig.4). Asymmetric peaks, also located at a non-zero bias, have been observed in the tunneling conductance at the vortex center in  $\text{LiFeAs}$  [14], in  $(\text{Ba}_{0.6}\text{K}_{0.4})\text{Fe}_2\text{As}_2$  [20] and in  $\text{YNi}_2\text{B}_2\text{C}$ [42]. The peak not located exactly at zero bias is explained by invoking non-negligible values of  $\Delta^2/2E_F$ . To obtain values of  $\Delta^2/2E_F$  of the order of the mV, one requires  $k_F\xi$  of order of one. Significant mass enhancements have been observed in a variety of measurements in  $\text{BaFe}_2(\text{As}_{1-x}\text{P}_x)_2$  close to optimal doping[45, 46]. Furthermore, estimations of  $E_F$  from superfluid density measurements lead to values in the range of a few hundreds K[47]. All this suggests that  $k_F\xi$  might be indeed close to one in some of these systems. However, the role of the multiband structure of the Fermi surface in these systems



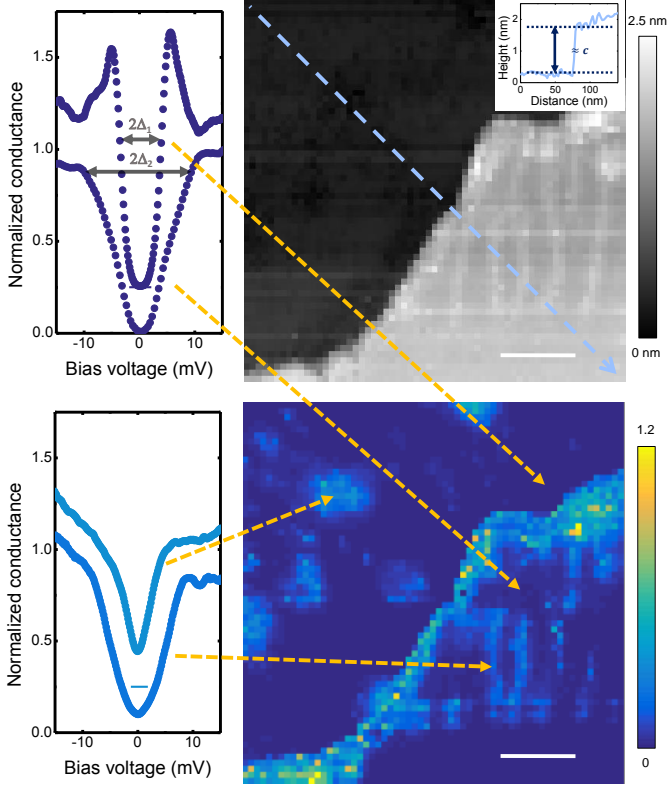


FIG. 8. The top right panel: the topography with the color scale as indicated by the bar on the right. The profile along the blue arrow in the image is shown in the inset. The step height is of order of the unit cell  $c$ -axis size, marked by a black arrow in the inset. The bottom right panel: zero bias normalized conductance map in the same area, with the color scale given by the bar on the right. White bars are 20 nm long. Tunneling conductance curves in different areas are given in the left panels. These are shifted for clarity, providing the zero conductance position by blue horizontal bars.

has not been taken into account with detail. Furthermore, the conductance at the peak in  $\text{CaKFe}_4\text{As}_4$  has a comparatively small value. Finally, note that the peak in  $\text{CaKFe}_4\text{As}_4$  is located at positive values of the bias voltage (tunneling into empty states of the sample), whereas it occurs at negative bias voltages in  $(\text{Ba}_{0.6}\text{K}_{0.4})\text{Fe}_2\text{As}_2$  and in  $\text{LiFeAs}$  (tunneling into occupied states of the sample). All this suggests that the influence of the bandstructure and of electronic scattering on the vortex core levels has to be examined in more detail.

#### D. Tunneling conductance of pinned vortices.

To pursue the role of core levels further, we show in Fig. 9, a vortex pinned along a line associated to a linear defect that gives a finite zero bias conductance at 1 T. The arrow in middle panels crosses this line. We find in there an increased zero bias conductance. The lateral size

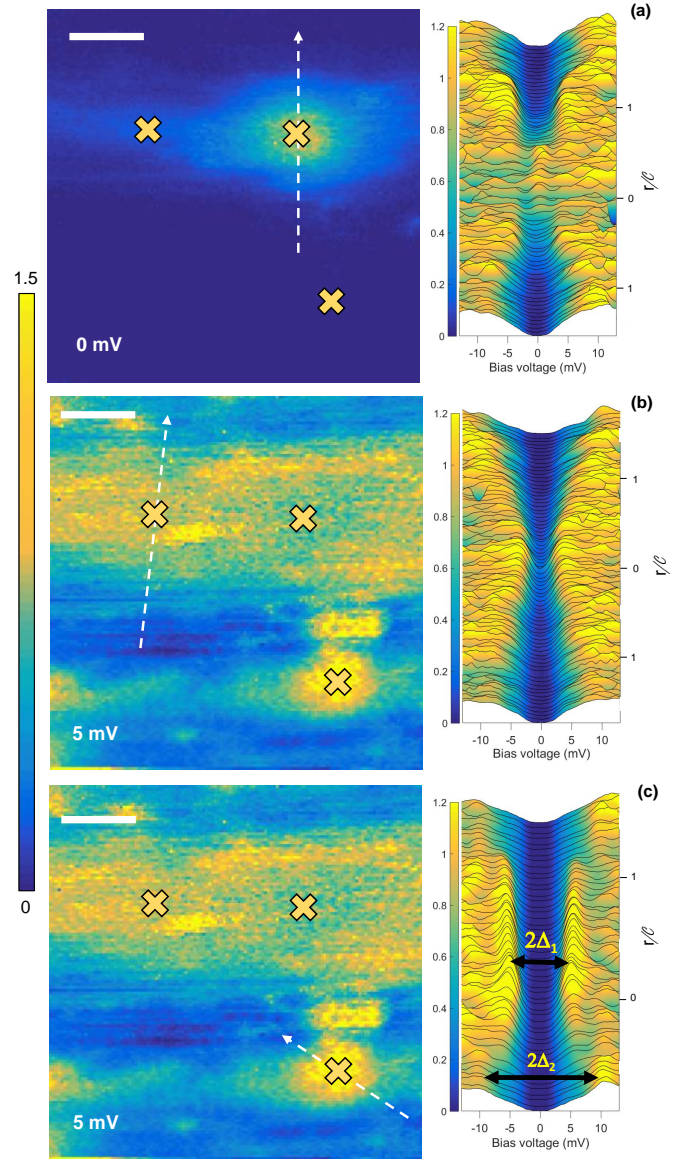


FIG. 9. Left panels show normalized conductance maps at zero bias (top panel) and at 5 mV (middle and bottom panels). In the right panels we show normalized tunneling conductance vs bias voltage along the lines marked by dashed white arrows in the left panels. Crosses provide the centers of the three lines. Color bars provide the scale in the normalized tunneling conductance. Length scale is given by the white bar, which is 10 nm long. The right scale provides the distance along the dashed lines in units of the core size  $C$ , the zero corresponding to the position of the crosses in the left panels. All figures are for  $H = 1\text{ T}$ .

of the line with a finite zero bias conductance is similar to the vortex core size  $C_i$ .

We also highlight a spot appearing at finite bias voltages below the vortex in the lower panels. The spot is not visible in the zero bias conductance maps (upper panel) but appears most clearly at  $\pm 5\text{ mV}$ . In this spot, we mea-

sure mostly curves showing the features corresponding to the smaller sized superconducting gap. The positions of surrounding vortices (not shown) suggest that the vortex might be located in the lower part of the figure, instead on the line with a zero bias conductance. In spite of that, the vortex remains in the line. Notice that the area showing smaller sized superconducting gap (lower panels of Fig. 9) also shows sizeable modifications of the tunneling conductance with respect to the rest of the image. The vortex is not, however, attracted to that position. The vortex prefers to be located at the area with a finite zero bias conductance. The position within the line is determined by the position of other vortices located along the same line which are at a distance of approximately the intervortex distance at this magnetic field (50 nm, not shown). This suggests that the vortex position within each line is due to intervortex repulsion.

### E. Obtaining the vortex core radius $\mathcal{C}$

To obtain the magnetic field dependence of the vortex core radius  $\mathcal{C}$ , we take zero bias conductance maps of vortices that have a round shape and are far from pinning centers. We then center the image at a single vortex and make the angular average of the tunneling conductance for each distance  $r$  from the vortex center. We define the normalized conductance as

$$\sigma = \frac{\sigma_0(r) - \sigma_0(r^*)}{\sigma_0(0) - \sigma_0(r^*)}. \quad (1)$$

where  $\sigma$  is the normalized conductance shown in the Fig.4,  $\sigma_0$  the angular average of the tunneling conductance,  $r$  the distance from the vortex center and  $r^*$  is the distance from the vortex center to the center of a vortex triangle. The equations used for the fits are described in Ref.[26].

### F. Experimental details

We grow single crystals of  $\text{CaKFe}_4\text{As}_4$  from FeAs flux, using As (99.9999%), K (99.95%) and Fe (99.9+%) from Alpha Aesar, and Ca from Ames Laboratory materials preparation center (99.9%), following the procedure describe in Ref.[17]. Single crystals are screened to make sure that they are single phase, as in Refs.[17–19] and have a shiny flat surface. Their crystals are plate like of several millimeters size and several hundreds of microns thick. Their crystallographic c-axis is perpendicular to the plate. To make the STM measurements, we use a sliding sample holder, described in Ref.[48]. We position a copper beam in the path of the sample holder, in such a way that the sample holder glides below the beam. We then glue the sample on the sample holder and a brass stick on top of the sample, in such a way that the sample remains below the beam but the stick is pushed by the beam when moving the sample holder. We use silver epoxy to glue the sample and Araldite to glue the stick. We then cool down to 4.2 K and move the sample holder. The stick is then pushed by the beam and flies to the bottom of the vacuum chamber of the cryostat. Part of the surface of the sample remains glued to the stick, so that the remaining sample is nicely cleaved in-situ. When heating up again after the experiment, we observe an optically clean flat and nicely shining surface.

The base temperature of our cryogenic system is of 800 mK and our resolution in energy of  $13 \mu\text{eV}$ [49]. We use a tip of gold. Close to the sample, we also glue a flat piece of gold. We can then use the gliding sample holder to position the tip on top of the gold sample to clean and regenerate the tip in-situ using the methods described in Refs.[50]. In addition, we can change the scanning window in-situ, as described in Ref.[48], and have been able to study many different surfaces. Magnetic fields are applied parallel to the c-axis. As usual, the tunneling conductance is normalized by its value at a bias voltage far from the superconducting features.

- 
- [1] Y. Kamihara, T. Watanabe, M. Hirano, and H. Hosono, “Iron-based layered superconductor  $\text{La}[\text{O}_{1-x}\text{F}_x]\text{FeAs}$  ( $x = 0.05\text{--}0.12$ ) with  $T_c = 26$  K,” *Journal of the American Chemical Society* **130**, 3296–3297 (2008).
  - [2] P. C. Canfield and S. L. Bud’ko, “FeAs-based superconductivity: A case study of the effects of transition metal doping on  $\text{BaFe}_2\text{As}_2$ ,” *Annual Review of Condensed Matter Physics* **1**, 27–50 (2010).
  - [3] J. Paglione and R. L. Greene, “Manifesto for a higher  $T_c$ ,” *Nature Physics* **6**, 645–658 (2010).
  - [4] P. J. Hirschfeld, M. M. Korshunov, and I. I. Mazin, “Gap symmetry and structure of Fe-based superconductors,” *Reports on Progress in Physics* **74**, 124508 (2011).
  - [5] D. V. Efremov, M. M. Korshunov, O. V. Dolgov, A. A. Golubov, and P. J. Hirschfeld, “Disorder-induced transition between  $s_{\pm}$  and  $s_{++}$  states in two-band superconductors,” *Phys. Rev. B* **84**, 180512 (2011).
  - [6] H. Hosono and K. Kuroki, “Iron-based superconductors: Current status of materials and pairing mechanism,” *Physica C: Superconductivity and its Applications* **514**, 399 – 422 (2015).
  - [7] V. G. Kogan, “Pair breaking in iron pnictides,” *Phys. Rev. B* **80**, 214532 (2009).
  - [8] P. J. Hirschfeld, “Using gap symmetry and structure to reveal the pairing mechanism in Fe-based superconductors,” *Comptes Rendus Physique* **17**, 197 – 231 (2016).
  - [9] K. Cho, M. Konczykowski, S. Teknowijoyo, M. A. Tanatar, Y. Liu, T. A. Lograsso, W. E. Straszheim, V. Mishra, S. Maiti, P. J. Hirschfeld, and R. Prozorov, “Energy Gap Evolution Across the Superconductivity Dome in Single Crystals of  $(\text{Ba}_{1-x}\text{K}_x)\text{Fe}_2\text{As}_2$ ,” (2016), cond-mat.supr-con/1605.04183v1.
  - [10] H. Suderow, S. Kambe, J. P. Brison, A. Huxley, J. Flouquet, and F. Rullier-Albenque, “Controlled creation of

- structural defects in the heavy fermion superconductor UPt<sub>3</sub> and its influence on the superconducting properties,” *Journal of Low Temperature Physics* **116**, 393–405 (1999).
- [11] F. Massee, P. O. Sprau, Y.-L. Wang, J. C. S. Davis, G. Ghigo, G. D. Gu, and W.-K. Kwok, “Imaging atomic-scale effects of high-energy ion irradiation on superconductivity and vortex pinning in Fe(Se,Te),” *Science Advances* **1** (2015), 10.1126/sciadv.1500033.
- [12] C.-L. Song, Y.-L. Wang, Y.-P. Jiang, L. Wang, K. He, X. Chen, J. E. Hoffman, X.-C. Ma, and Q.-K. Xue, “Suppression of superconductivity by twin boundaries in FeSe,” *Phys. Rev. Lett.* **109**, 137004 (2012).
- [13] J. E. Hoffman, “Spectroscopic scanning tunneling microscopy insights into Fe-based superconductors,” *Reports on Progress in Physics* **74**, 124513 (2011).
- [14] T. Hanaguri, K. Kitagawa, K. Matsubayashi, Y. Mazaki, Y. Uwatoko, and H. Takagi, “Scanning tunneling microscopy/spectroscopy of vortices in LiFeAs,” *Phys. Rev. B* **85**, 214505 (2012).
- [15] M. P. Allan, A. W. Rost, A. P. Mackenzie, Y. Xie, J. C. Davis, K. Kihou, C. H. Lee, A. Iyo, H. Eisaki, and T. M. Chuang, “Anisotropic energy gaps of iron-based superconductivity from intraband quasiparticle interference in LiFeAs,” *Science* **336**, 563–567 (2012).
- [16] A. Iyo, K. Kawashima, T. Kinjo, T. Nishio, S. Ishida, H. Fujihisa, Y. Gotoh, K. Kihou, H. Eisaki, and Y. Yoshida, “New-structure-type Fe-based superconductors: CaAF<sub>4</sub>As<sub>4</sub> (A = K, Rb, Cs) and SrAF<sub>4</sub>As<sub>4</sub> (A = Rb, Cs),” *Journal of the American Chemical Society* **138**, 3410–3415 (2016).
- [17] W. R. Meier, U. S. Kaluarachchi T. Kong, V. Taufour, N. H. Jo, G. Drachuck, A. E. Böhmer, S. M. Saunders, A. Sapkota, A. Kreyssig, M. A. Tanatar, R. Prozorov, A. I. Goldman, F.F. Balakirev, A. Gurevich, S. L. Budko, and P. C. Canfield, “Anisotropic thermodynamic and transport properties of single crystalline CaKFe<sub>4</sub>As<sub>4</sub>,” (2016), cond-mat.supr-con/1605.05617v2.
- [18] K. Cho and A. Fente and S. Teknowijoyo and M. A. Tanatar and T. Kong, W. Meier and U. Kaluarachchi and I. Guillamón and H. Suderow and S. L. Bud’ko and P. C. Canfield and R. Prozorov, “Nodeless multiband superconductivity in stoichiometric single crystalline CaKFe<sub>4</sub>As<sub>4</sub>,” (2016), cond-mat.supr-con/1606.06245v1.
- [19] D. Mou, T. Kong, W. R. Meier, F. Lochner, L.-L. Wang, Q. Lin, Y. Wu, S.L. Bud’ko, I. Eremin, D.D. Johnson, P.C. Canfield, and A. Kaminski, “Enhancement of the superconducting gap by nesting in CaKFe<sub>4</sub>As<sub>4</sub> - a new high temperature superconductor,” (2016), cond-mat.supr-con/1606.05643.
- [20] L. Shan, Y. L. Wang, B. Shen, B. Zeng, Y. Huang, A. Li, D. Wang, H. Yang, C. Ren, Q. H. Wang, S. H. Pan, and H. H. Wen, “Observation of ordered vortices with andreev bound states in Ba<sub>0.6</sub>K<sub>0.4</sub>Fe<sub>2</sub>As<sub>2</sub>,” *Nature Physics* **7**, 325–331 (2011).
- [21] H. Suderow, I. Guillamón, J. G. Rodrigo, and S. Vieira, “Imaging superconducting vortex cores and lattices with a scanning tunneling microscope,” *Superconductor Science and Technology* **27**, 063001 (2014).
- [22] Y. Yin, M. Zech, T. L. Williams, X. F. Wang, G. Wu, X. H. Chen, and J. E. Hoffman, “Scanning tunneling spectroscopy and vortex imaging in the iron pnictide superconductor BaFe<sub>1.8</sub>Co<sub>0.2</sub>As<sub>2</sub>,” *Phys. Rev. Lett.* **102**, 097002 (2009).
- [23] F. Massee, Y. Huang, R. Huisman, S. de Jong, J. B. Goedkoop, and M. S. Golden, “Nanoscale superconducting-gap variations and lack of phase separation in optimally doped BaFe<sub>1.86</sub>Co<sub>0.14</sub>As<sub>2</sub>,” *Phys. Rev. B* **79**, 220517 (2009).
- [24] Ø. Fischer, M. Kugler, I. Maggio-Aprile, C. Berthod, and C. Renner, “Scanning tunneling spectroscopy of high-temperature superconductors,” *Rev. Mod. Phys.* **79**, 353–419 (2007).
- [25] C.-L. Song, Y. Yin, M. Zech, T. Williams, Michael M. Yee, G.-F. Chen, J.-L. Luo, N.-L. Wang, E. W. Hudson, and J. E. Hoffman, “Dopant clustering, electronic inhomogeneity, and vortex pinning in iron-based superconductors,” *Phys. Rev. B* **87**, 214519 (2013).
- [26] A. Fente, E. Herrera, I. Guillamón, H. Suderow, S. Mañas-Valero, M. Galbiati, E. Coronado, and V.G. Kogan, “Field dependence of the vortex core size probed by STM,” (2016), cond-mat.supr-con/1606.00302.
- [27] V. G. Kogan and N. V. Zhelezina, “Field dependence of the vortex core size,” *Phys. Rev. B* **71**, 134505 (2005).
- [28] J. E. Sonier, “Investigations of the core structure of magnetic vortices in type-II superconductors using muon spin rotation,” *Journal of Physics: Condensed Matter* **16**, S4499 (2004).
- [29] E. Herrera, I. Guillamón, J. A. Galvis, A. Correa, A. Fente, R. F. Lucas, F. J. Mompean, M. García-Hernández, S. Vieira, J. P. Brison, and H. Suderow, “Magnetic field dependence of the density of states in the multiband superconductor  $\beta$ -Bi<sub>2</sub>Pd,” *Phys. Rev. B* **92**, 054507 (2015).
- [30] M. R. Eskildsen, M. Kugler, S. Tanaka, J. Jun, S. M. Kazakov, J. Karpinski, and Ø. Fischer, “Vortex imaging in the  $\pi$ -band of magnesium diboride,” *Phys. Rev. Lett.* **89**, 187003 (2002).
- [31] M. R. Eskildsen, N. Jenkins, G. Levy, M. Kugler, Ø. Fischer, J. Jun, S. M. Kazakov, and J. Karpinski, “Vortex imaging in magnesium diboride with  $h_c$ ,” *Phys. Rev. B* **68**, 100508 (2003).
- [32] F. Giubileo, F. Bobba, A. Scarfato, A. M. Cucolo, A. Kohen, D. Roditchev, N. D. Zhigadlo, and J. Karpinski, “Local tunneling study of three-dimensional order parameter in the  $\pi$  band of Al-doped MgB<sub>2</sub> single crystals,” *Phys. Rev. B* **76**, 024507 (2007).
- [33] E. Boaknin, M. A. Tanatar, J. Paglione, D. Hawthorn, F. Ronning, R. W. Hill, M. Sutherland, L. Taillefer, J. Sonier, S. M. Hayden, and J. W. Brill, “Heat conduction in the vortex state of NbSe<sub>2</sub>: Evidence for multiband superconductivity,” *Phys. Rev. Lett.* **90**, 117003 (2003).
- [34] I. Guillamón, R. Córdoba, J. Sesé, J. M. De Teresa, M. R. Ibarra, S. Vieira, and H. Suderow, “Enhancement of long-range correlations in a 2D vortex lattice by an incommensurate 1D disorder potential,” *Nature Physics* **10**, 851–856 (2015).
- [35] J.-X. Yin, Zheng Wu, J.-H. Wang, Z.-Y. Ye, J. Gong, X.-Y. Hou, L. Shan, A. Li, X.-J. Liang, X.-X. Wu, J. Li, C.-S. Ting, Z.-Q. Wang, J.-P. Hu, P.-H. Hor, H. Ding, and S.H. Pan, “Observation of a robust zero-energy bound state in iron-based superconductor Fe(Te,Se),” *Nature Physics* **11**, 543–546 (2015).
- [36] S. Grothe, S. Chi, P. Dosanjh, R. Liang, W. N. Hardy, S. A. Burke, D. A. Bonn, and Y. Pennec, “Bound states of defects in superconducting LiFeAs studied by scanning tunneling spectroscopy,” *Phys. Rev. B* **86**, 174503 (2012).



- [37] S. Chi, S. Johnston, G. Levy, S. Grothe, R. Szedlak, B. Ludbrook, R. Liang, P. Dosanjh, S. A. Burke, A. Damascelli, D. A. Bonn, W. N. Hardy, and Y. Pennec, “Sign inversion in the superconducting order parameter of LiFeAs inferred from Bogoliubov quasiparticle interference,” *Phys. Rev. B* **89**, 104522 (2014).
- [38] A. Fente *et al.*, “Scanning probe microscopy of strain dependent superconductivity in  $\text{Ca}(\text{Fe}_{0.97}\text{Co}_{0.03})\text{As}_2$ ,” (2016), to be published.
- [39] S. Ran, S. L. Bud’ko, D. K. Pratt, A. Kreyssig, M. G. Kim, M. J. Kramer, D. H. Ryan, W. N. Rowan-Weetaluktuk, Y. Furukawa, B. Roy, A. I. Goldman, and P. C. Canfield, “Stabilization of an ambient-pressure collapsed tetragonal phase in  $\text{CaFe}_2\text{As}_2$  and tuning of the orthorhombic-antiferromagnetic transition temperature by over 70 K via control of nanoscale precipitates,” *Phys. Rev. B* **83**, 144517 (2011).
- [40] H. F. Hess, R. B. Robinson, and J. V. Waszczak, “Vortex-core structure observed with a scanning tunneling microscope,” *Phys. Rev. Lett.* **64**, 2711–2714 (1990).
- [41] I. Guillamon, H. Suderow, F. Guinea, and S. Vieira, “Intrinsic atomic-scale modulations of the superconducting gap of  $2\text{H-NbSe}_2$ ,” *Phys. Rev. B* **77**, 134505 (2008).
- [42] H. Nishimori, K. Uchiyama, S.-I. Kaneko, A. Tokura, H. Takeya, K. Hirata, and N. Nishida, “First observation of the fourfold-symmetric and quantum regime vortex core in  $\text{YNi}_2\text{B}_2\text{C}$  by scanning tunneling microscopy and spectroscopy,” *Journal of the Physical Society of Japan* **73**, 3247–3250 (2004).
- [43] I. Guillamón, H. Suderow, S. Vieira, L. Cario, P. Diener, and P. Rodière, “Superconducting density of states and vortex cores of  $2\text{H-NbSe}_2$ ,” *Phys. Rev. Lett.* **101**, 166407 (2008).
- [44] C. Caroli, P.G. De Gennes, and J. Matricon, “Bound fermion states on a vortex line in a type II superconductor,” *Physics Letters* **9**, 307 – 309 (1964).
- [45] K. Hashimoto, K. Cho, T. Shibauchi, S. Kasahara, Y. Mizukami, R. Katsumata, Y. Tsuruhara, T. Terashima, H. Ikeda, M. A. Tanatar, H. Kitano, N. Salovich, R. W. Giannetta, P. Walmsley, A. Carrington, R. Prozorov, and Y. Matsuda, “A sharp peak of the zero-temperature penetration depth at optimal composition in  $\text{BaFe}_2(\text{As}_{1-x}\text{P}_x)_2$ ,” *Science* **336**, 1554–1557 (2012).
- [46] P. Walmsley, C. Putzke, L. Malone, I. Guillamón, D. Vignolles, C. Proust, S. Badoux, A. I. Coldea, M. D. Watson, S. Kasahara, Y. Mizukami, T. Shibauchi, Y. Matsuda, and A. Carrington, “Quasiparticle mass enhancement close to the quantum critical point in  $\text{BaFe}_2\text{As}_{1-x}\text{P}_x)_2$ ,” *Phys. Rev. Lett.* **110**, 257002 (2013).
- [47] K. Hashimoto, Y. Mizukami, R. Katsumata, H. Shishido, M. Yamashita, H. Ikeda, Y. Matsuda, J. A. Schlueter, J. D. Fletcher, A. Carrington, D. Gnida, D. Kaczorowski, and T. Shibauchi, “Anomalous superfluid density in quantum critical superconductors,” *Proceedings of the National Academy of Sciences* **110**, 3293–3297 (2013).
- [48] H. Suderow, I. Guillamon, and S. Vieira, “Compact very low temperature scanning tunneling microscope with mechanically driven horizontal linear positioning stage,” *Review of Scientific Instruments* **82**, 033711 (2011).
- [49] I. Guillamon, H. Suderow, S. Vieira, and P. Rodiere, “Scanning tunneling spectroscopy with superconducting tips of Al,” *Physica C: Superconductivity and its Applications* **468**, 537 – 542 (2008).
- [50] J. G. Rodrigo, H. Suderow, S. Vieira, E. Bascones, and F. Guinea, “Superconducting nanostructures fabricated with the scanning tunnelling microscope,” *Journal of Physics: Condensed Matter* **16**, R1151 (2004).